Depth from motion algorithm and hardware architecture for smart cameras

Abiel Aguilar-González, Miguel Arias-Estrada, François Berry

MDPI

Article

Depth from motion algorithm and hardware architecture for smart cameras

Abiel Aguilar-González [1,2*], Miguel Arias-Estrada [1] and François Berry [2,]

[1] Instituto Nacional de Astrofísica, Óptica y Electrónica (INAOE), Tonantzintla, Mexico
[2] Institut Pascal, Université Clermont Auvergne (UCA), Clermont-Ferrand, France
* Correspondence: abiel@inaoep.mx, abiel.aguilar_gonzalez@etu.uca.fr

Academic Editor: name
Version November 26, 2018 submitted to Sensors

Abstract: Applications such as autonomous navigation, robot vision, autonomous flying, etc., require depth map information of the scene. Depth can be estimated by using a single moving camera (depth from motion). However, traditional depth from motion algorithms have low processing speed and high hardware requirements that limits the embedded capabilities. In this work, we propose a hardware architecture for depth from motion that consists of a flow/depth transformation and a new optical flow algorithm. Our optical flow formulation consists in an extension of the stereo matching problem. A pixel-parallel/window-parallel approach where a correlation function based in the Sum of Absolute Differences computes the optical flow is proposed. Further, in order to improve the Sum of Absolute Differences performance, the curl of the intensity gradient as preprocessing step is proposed. Experimental results demonstrated that it is possible to reach higher accuracy (90% of accuracy) compared with previous FPGA-based optical flow algorithms. For the depth estimation, our algorithm delivers dense maps with motion and depth information on all the image pixels, with a processing speed up to 128 times faster than previous works and making it possible to achieve high performance in the context of embedded applications.

Keywords: Depth estimation; monocular systems; optical flow; smart cameras; FPGA

1. Introduction

Smart cameras are machine vision systems which, in addition to image capture circuitry, are capable of extracting application-specific information from the captured images. For example, for video surveillance, image processing algorithms implemented inside the camera fabric could detect and track pedestrians [1], but for a robotic application, computer vision algorithms could estimate the system egomotion [2]. In recent years, advances in embedded vision systems such as progress in microprocessor power and FPGA technology allowed the creation of compact smart cameras with increased performance for real world applications [3–6]. As result, in current embedded applications, image processing algorithms inside the smart cameras fabric deliver an efficient on-board solution for: motion detection [7], object detection/tracking [8,9], inspection and surveillance [10], human behavior recognition [11], etc. Another algorithm that could be highly used by smart cameras are computer vision algorithms since they are the basis of several applications (automatic inspection, controlling processes, detecting events, modeling objects or environments, navigation and so on). Unfortunately, mathematical formulation of computer vision algorithms is not compliant with the hardware technologies (FPGA/CUDA) often used in smart cameras. In this work, we are interested in depth estimation from monocular sequences in the context of a smart camera because depth is the basis to obtain useful scene abstractions, for example: 3D reconstructions of the world and the camera egomotion.

1.1. Depth estimation from monocular sequences

In several applications, like autonomous navigation [12], robot vision and surveillance [1], autonomous flying [13], etc., there is a need for determining the depth map of the scene. Depth can be estimated by using stereo cameras [14], by changing focal length [15], or by employing a single moving camera [16]. In this work we are interested in depth estimation from monocular sequences by using a single moving camera (depth from motion). This choice is motivated because monocular systems have higher efficiency compared with other approaches, simpler and more accurate than defocus techniques and, cheaper/smaller compared with stereo-based techniques. In monocular systems, depth information can be estimated based on two or multiple frames of a video sequence. For two frames, image information may not provide sufficient information for accurate depth estimation. The use of multiple frames improves the accuracy, reduces the influence of noise and allows the extraction of additional information which cannot be recovered from just two frames, but the system complexity and computational cost is increased. In this work, we use information from two consecutive frames of the monocular sequence since our algorithm is focused for smart cameras and in this context hardware resources are limited.

1.2. Motivation and scope

In the last decade several works have demonstrated that depth information is highly useful for embedded robotic applications [1,12,13]. Unfortunately, depth information estimation is a relatively complex task. In recent years, the most popular solution is the use of active vision to estimate depth information from the scene [17–21], i.e., LIDAR sensors or RGBD cameras that can deliver accurate depth maps in real time, however they increase the systems size and cost. In this work, we propose a new algorithm and an FPGA hardware architecture for depth estimation. First, a new optical flow algorithm estimates the motion (flow) at each point in the input image. Then, a flow/depth transformation computes the depth in the scene. For the optical flow algorithm: an extension of the stereo matching problem is proposed. A pixel-parallel/window-parallel approach where a Sum of Absolute Differences computes the optical flow is implemented. Further, in order to improve the Sum of Absolute Differences performance, we propose the curl of the intensity gradient as preprocessing step. For the depth estimation proposes: we introduce a flow/depth transformation inspired in the epipolar geometry.

2. Related work

In previous works, depth estimation is often estimated by using a single moving camera. This approach is called depth from motion and consists in computing the depth from the pixel velocities inside the scene (optical flow). i.e., optical flow is the basis for depth from motion.

2.1. FPGA architectures for optical flow

In [22], a hardware implementation of a high complexity algorithm to estimate the optical flow from image sequences in real time is presented. In order to fulfil with the architectural limitations, the original gradient-based optical flow was modified (using a smoothness constraint for decreasing iterations). The developed architecture can estimate the optical flow in real time and can be constructed with FPGA or ASIC devices. However, due to the mathematical limitations of the CPU formulation (complex/iterative operations), speed processing is low, compared with other FPGA-based architectures for real-time image processing [23,24]. In [25], a pipelined optical-flow processing system that works as a virtual motion sensor is described. The proposed approach consists of several spatial and temporal filters (Gaussian and gradient spatial filters and IIR temporal filter) implemented in cascade. The proposed algorithm was implemented in an FPGA device, enabling the easy change of the configuration parameters to adapt the sensor to different speeds, light conditions and other environmental factors. This makes possible the implementation of an FPGA-based smart camera for

optical flow. In general, the proposed architecture reaches a reasonable hardware resources usage but accuracy and processing speed is low (lower than 7 fps for 640×480 image resolution). In [26], a tensor-based optical flow algorithm is presented. This algorithm was developed and implemented using FPGA technology. Experimental results demonstrated high accuracy compared with previously FPGA-based algorithms for optical flow. In addition, the proposed design can process 640×480 images at 64 fps with a relatively low resource requirement, making it easier to fit into small embedded systems. In [27], a highly parallel architecture for motion estimation is presented. The developed FPGA-architecture implements the Lucas and Kanade algorithm [28] with the multi-scale extension for the computation of large motion estimations in an FPGA. Although the proposed architecture reaches a low hardware requirement with a high processing speed, the use of huge external memory capacity is needed. Further, in order to fulfil with the hardware limitations, the accuracy is low (near 11% more error compared with the original CPU version of the Lukas and Kanade algorithm). Finally, in [29], an FPGA-based platform with the capability of calculating real-time optical flow at 127 frames per second for a 376×240 pixel resolution is presented. Radial undistortion, image rectification, disparity estimation and optical flow calculation tasks are performed on a single FPGA without the need of external memory. So, the platform is perfectly suited for mobile robots or embedded applications. Unfortunately, accuracy is low (qualitatively lower accuracy than CPU based approaches).

2.2. Optical flow methods based in learning techniques

There are some recent works that addresses the optical flow problem via learning techniques [30]. In 2015 [31] proposed the use of convolutional neuronal networks (CNNs) as an alternative framework to solve the optical flow estimation problem. Two different architectures were proposed and compared: a generic architecture and another one including a layer that correlates feature vectors at different image locations. Experimental results demonstrated a competitive accuracy at frame rates of 5 to 10 fps. On the other hand, in 2017 [32] developed a stacked architecture that includes warping of the search image with intermediate optical flow. Further, in order to achieve high accuracy on small displacements, authors introduced a sub-network specializing on small motions. Experimental results demonstrated that it is possible to reach more than 95% of accuracy, decreasing the estimation error by more than 50% compared with previous works.

3. The proposed algorithm

In **Fig.** 1 an overview of our algorithm is shown. First, given an imager as sensor, two consecutive frames $(f_t(x,y),\ f_{t+1}(x,y))$ are stored in local memory. Then, an optical flow algorithm computes 2D pixel displacements between $f_t(x,y)$ and $f_{t+1}(x,y)$. A dynamic template based on the optical flow previously computed $(\Delta_{x,t-1}(x,y),\ \Delta_{y,t-1}(x,y))$ computes the search region size for the current optical flow. Then, let the optical flow for the current frame be $(\Delta_x(x,y),\ \Delta_y(x,y))$, the final step is depth estimation for all the pixels in the reference image $D(x,y)$. In the following subsections, details about the proposed algorithm are presented.

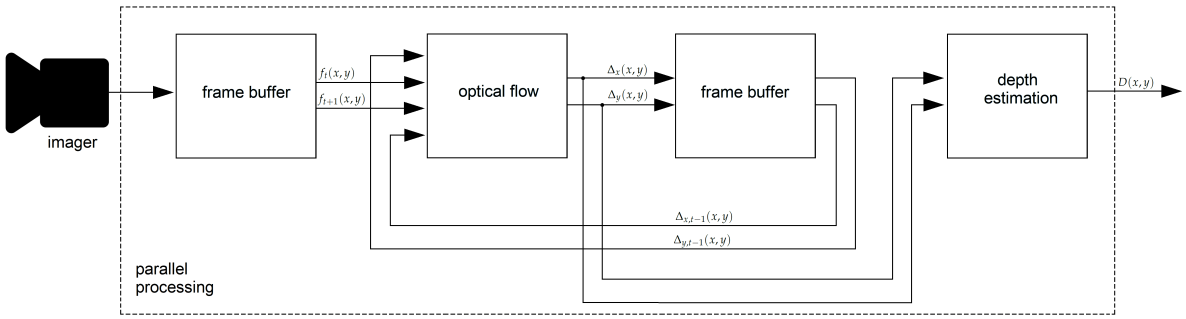

Figure 1. Block diagram of the proposed algorithm

3.1. Frame buffer

The first step in our mathematical formulation is image storage, considering that in most cases the imager provides data as a stream, some storage is required in order to have two consecutive frames available at the same time t. More information/details about the storage architecture are presented in **Section** 4.1. For mathematical formulation, we consider the first frame (frame at t time) as $f_t(x,y)$ while the second frame (frame at $t+1$ time) is $f_{t+1}(x,y)$.

3.2. Optical flow

In previous works, iterative algorithms, such as the Lucas Kanade [28] or the Horn–Schunck [33] algorithms have been used on order to compute optical flow across video sequences, then, given dense optical flow, geometric methods allow to compute the depth in the scene. However, these algorithms [28,33] have iterative operations that limit the performance for smart camera implementations. In order to avoid the iterative and convergence part of the traditional formulation we replace that with a correlation metric implemented inside a pixel-parallel/window-parallel formulation. In **Fig.** 2 an overview of our optical flow algorithm is shown. Let $(f_t(x,y), f_{t+1}(x,y)$ be two consecutive frames from a video sequence , curl of the intensity gradient $\frac{df(x,y)}{d\mathbf{x}}$ are computed, see **Eq.** 1, where ∇ is the **Del** operator. Let curl be a vector operator that describes the infinitesimal rotation, then, at every pixel the curl of that pixel is represented by a vector where attributes (length and direction) characterize the rotation at that point. In our case, we use only the norm of $\overline{\mathbf{Curl}}(x,y)$, as shown in **Eq.** 2 and, as illustrated in **Fig.** 3 . This operation increases the robustness under image degradations (color/texture repetition, illumination changes, noise), therefore, simple similarity metrics [34] deliver accurate pixel tracking, simpler than previous tracking algorithms [28,33]. Given the curl images for two consecutive frames $(\overline{\mathbf{Curl}}_t(x,y), \overline{\mathbf{Curl}}_{t+1}(x,y)$, dense optical flow $(\Delta_x(x,y),\ \Delta_y(x,y)$, illustrated in **Fig.** 4) in the reference image is computed as shown in **Fig.** 5. This process assumes that pixel displacements between frames is such as it exists an overlap on two successive "search regions". A search region is defined as a patch around a pixel to track. Considering that between f_t and f_{t+1}, the image degradation is low, any similarity-based metric have to provide good accuracy. In our case, this similarity is calculated by a SAD (Sum of Absolute Difference). This process is defined in **Eq.** 3; where r is the patch size (see **Fig.** 5). $(\overline{\mathbf{Curl}}_t(x,y), \overline{\mathbf{Curl}}_{t+1}(x,y))$ are curl images on two consecutive frames. x,y are the spatial coordinates of pixels in f_t and, a,b are the spatial coordinates within a search region constructed in f_{t+1} (see **Eq.** 4 and 5); where $\Delta'_{x(t-1)}, \Delta'_{y(t-1)}$ are a dynamic search template, computed as shown in **Section** 3.3. k is the search size and s is a sampling value defined by the user. Finally, optical flow at the current time $(\Delta_x(x,y),\ \Delta_y(x,y))$ is computed by **Eq.** 6.

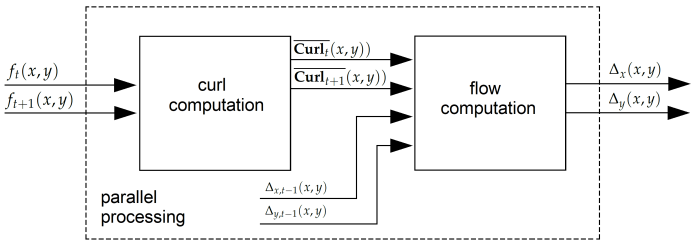

Figure 2. The optical flow step: first, curl images $(\overline{\mathbf{Curl}}_t(x,y))$, $(\overline{\mathbf{Curl}}_{t+1}(x,y))$ are computed. Then, given the curl images for two consecutive frames, pixels displacements $\Delta_x(x,y)$, $\Delta_y(x,y)$ (optical flow for all pixels in the reference image) are computed using a dynamic template based on the optical flow previously computed $(\Delta_{x,t-1}(x,y),\ \Delta_{y,t-1}(x,y))$.

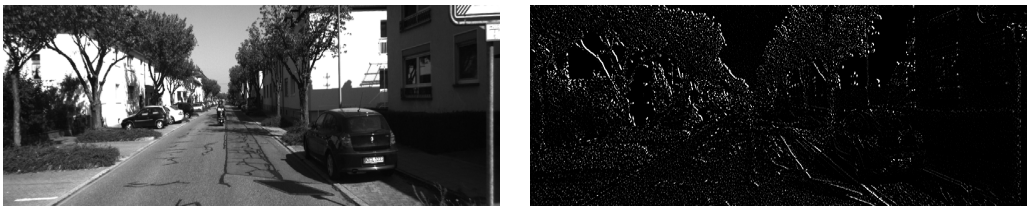

(a) input $(f(x,y))$ (b) output $\overline{\mathbf{Curl}}(x,y)$

Figure 3. Curl computation example. Input image taken from the KITTI benchmark dataset [35]

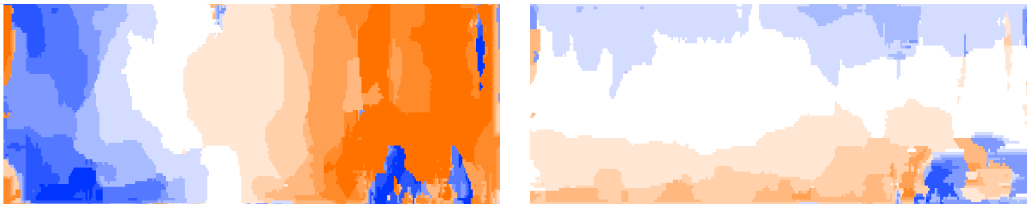

(a) $\Delta_x(x,y)$ (b) $\Delta_y(x,y))$

Figure 4. Optical flow example. Image codification as proposed in the Tsukuba benchmark dataset [36]

$$\mathbf{Curl}(x,y) = \nabla \times \frac{df(x,y)}{d\mathbf{x}} = \frac{\partial}{\partial y}\frac{\partial f(x,y)}{\partial x} - \frac{\partial}{\partial x}\frac{\partial f(x,y)}{\partial y} \tag{1}$$

$$\overline{\mathbf{Curl}}(x,y) = |\frac{\partial}{\partial y}\frac{\partial f(x,y)}{\partial x} - \frac{\partial}{\partial x}\frac{\partial f(x,y)}{\partial y}| \tag{2}$$

where

$$\frac{\partial f(x,y)}{\partial x} = G_x(x,y) = f(x+1,y) - f(x-1,y)$$
$$\frac{\partial f(x,y)}{\partial y} = G_y(x,y) = f(x,y+1) - f(x,y-1)$$
$$\frac{\partial}{\partial y}\frac{\partial f(x,y)}{\partial x} = G_x(x,y+1) - G_x(x,y-1)$$
$$\frac{\partial}{\partial x}\frac{\partial f(x,y)}{\partial y} = G_y(x+1,y) - G_y(x-1,y)$$

$$\mathrm{SAD}(a,b) = \sum_{u=-r}^{u=r}\sum_{v=-r}^{v=r} |\overline{\mathbf{Curl}_t}(x+u,y+v)| - |\overline{\mathbf{Curl}_{t+1}}(x+u+a,y+v+b)| \tag{3}$$

$$a = \Delta'_{x(t-1)}(x,y) - k : s : \Delta'_{x(t-1)}(x,y) + k \tag{4}$$

$$b = \Delta'_{y(t-1)}(x,y) - k : s : \Delta'_{y(t-1)}(x,y) + k \tag{5}$$

$$[\Delta_x(x,y), \Delta_y(x,y)] = \mathbf{arg\,min}_{(a,b)} SAD(a,b) \tag{6}$$

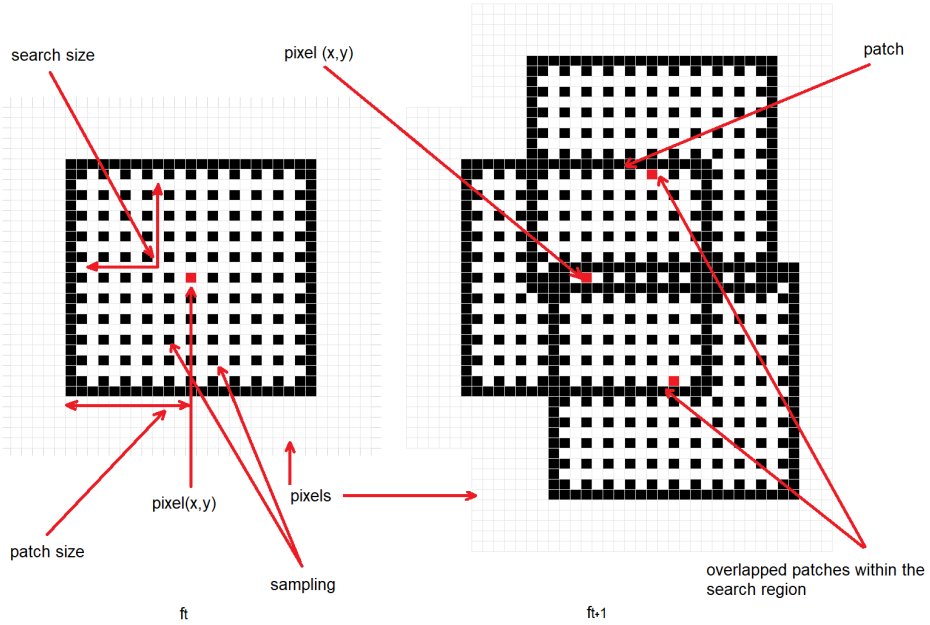

Figure 5. The proposed optical flow algorithm formulation: patch size = 10, search size = 10, sampling value = 2. For each pixel in the reference image f_t, n overlapped regions are constructed in f_{t+1}, n region center that minimizes or maximizes any similarity metric is the tracked position (flow) of the pixel (x, y) at f_{t+1}.

3.3. Search template

In optical flow, the search window size defines the maximum allowed motion to be detected in the sequence, see **Fig.** 4. In general, let p be a pixel in the reference image (f_t), whose 2D spatial location is defined as (x_t, y_t), the same pixel in the tracked image (f_{t+1}) has to satisfy $x_{t+1} \in x_t - k : 1 : x + k$, $y_{t+1} \in y - k : 1 : y_t + k$, where k is the search size for the tracking step. In practice, large search region sizes increase the tracking performance since feature tracking could be carried out in both slow and fast camera movements. However, large search sizes decrease the accuracy, i.e., if the search region size is equal to 1, then, $x_{t+1} \in x_t - 1 : 1 : x_t + 1$, $y_{t+1} \in y_t - 1 : 1 : y_t + 1$ so, there are 9 possible candidates for the tracking step and the mistake possibility is equal to 8, this considering that camera movement is slow and therefore pixel displacements between images are close to cero. In other scenario, if the search region size is equal to 10, then, $x_{t+1} \in x_t - 10 : 1 : x_t + 10$, $y_{t+1} \in y_t - 10 : 1 : y_t + 10$ so, there are 100 possible candidates for the tracking step and the mistake possibility is equal to 99. In our work, we propose to use the feedback of the previous optical flow step as a dynamic search size for the current step so, if camera movement in $t - 1$ is slow, small search sizes closer to the pixels being tracked (x_t, y_t) are used. On the other hand, given fast camera movements small search sizes far to the pixels being tracked are used. This makes the tracking step compute accurate results without outliers, furthermore, the use of small search sizes decreases the computational resources usage. For practical purposes we use a search region size equal to 10 since it provides a good tradeoff between robustness/accuracy and computational resources. So, let $\Delta_{x,t-1}(x, y)$, $\Delta_{y,t-1}(x, y)$ be the optical flow at time $t - 1$, the search template for the current time is computed as shown in **Eq.** 7 - 8, where k is the template size.

$$\Delta'_x(x+u, y+v) = \sum_{u=-k,v=-k}^{u=k,v=k} (\textbf{mean} \sum_{u=-k,v=-k}^{u=k,v=k} \Delta_{x,t-1}(x, y)) \tag{7}$$

$$\Delta'_y(x+u, y+v) = \sum_{u=-k,v=-k}^{u=k,v=k} (\textbf{mean} \sum_{u=-k,v=-k}^{u=k,v=k} \Delta_{y,t-1}(x,y)) \tag{8}$$

3.4. Depth estimation

In previous works it was demonstrated that monocular image sequences provide only partial information about the scene due to the computation of relative depth, unknown scale factor, etc. [37]. In order to recover the depth in the scene it is necessary to have assumptions about the scene and its 2-D images. In this work we assume that environment within the scene is rigid, then, given the optical flow of the scene (which represents pixel velocity across time), we suppose that depth in the scene is proportional to the pixel velocity. i.e., far objects have to be associated with a low velocity value while closer objects are associated with high velocity values. This could be considered as an extension of the epipolar geometry in which disparities values are proportional with the depth in the scene, as shown in **Fig.** 6.

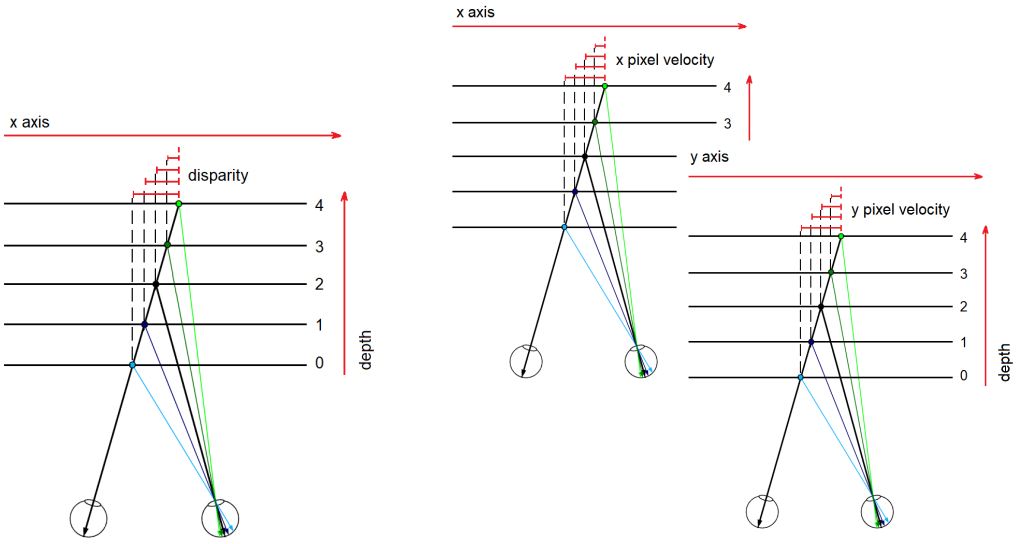

(a) depth from epipolar geometry (b) depth from motion

Figure 6. (a) Epipolar geometry: depth in the scene is proportional to the disparity value, i.e., far objects have low disparity values while closer objects are associated with high disparity values. To compute the disparity map (disparities for all pixels in the image) a stereo pair (two images with epipolar geometry) are needed. (b) Single moving camera: in this work we suppose that depth in the scene is proportional to the pixel velocity across the time. To compute the pixel velocity, optical flow across two consecutive frames has to be computed.

So, let $\Delta_x(x,y)$, $\Delta_y(x,y)$ be the optical flow (pixel velocity) at t time, depth in the scene $\textbf{depth}(x,y)$ is computed as proposed in **Eq.** 9, where $\textbf{depth}(x,y)$ is the norm of the optical flow. In **Fig.** 7 an example of depth map computed by the proposed approach is shown.

$$\textbf{depth}(x,y) = |||[\Delta_x(x,y), \Delta_y(x,y)]||| = \sqrt{\Delta_x(x,y)^2 + \Delta_y(x,y)^2} \tag{9}$$

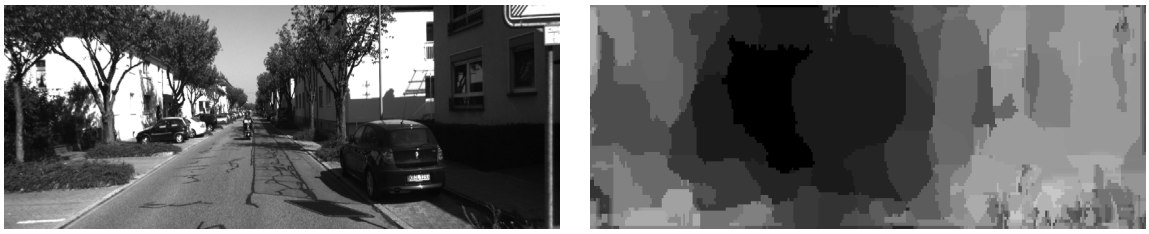

(a) input image (b) depth map

Figure 7. Depth estimation using the proposed algorithm

4. The FPGA architecture

In **Fig.** 8, an overview of the FPGA architecture for the proposed algorithm is shown. The architecture is centered on an FPGA implementation where all recursive/parallelizable operations are accelerated in the FPGA fabric. First, the "frame buffer" unit reads the pixel stream (pix [7:0]) delivered by the imager. In this block, frames captured by the imager are feed to/from an external DRAM memory and delivers pixel streams for two consecutive frames in parallel (pix1 [7:0], pix2 [7:0]). "Circular buffers" implemented inside the "Optical flow" unit are used to hold local sections of the frames that are being processed and allow for local parallel access that facilitates parallel processing. Finally, optical flow streams (pix3 [7:0], pix4 [7:0]) are used to computed the depth in the scene (pix7 [7:0]). In order to hold optical flow previously computed (which are used for the dynamic search template computation) a second "frame buffer" is used. In the following subsections details about the algorithm parallelization are shown.

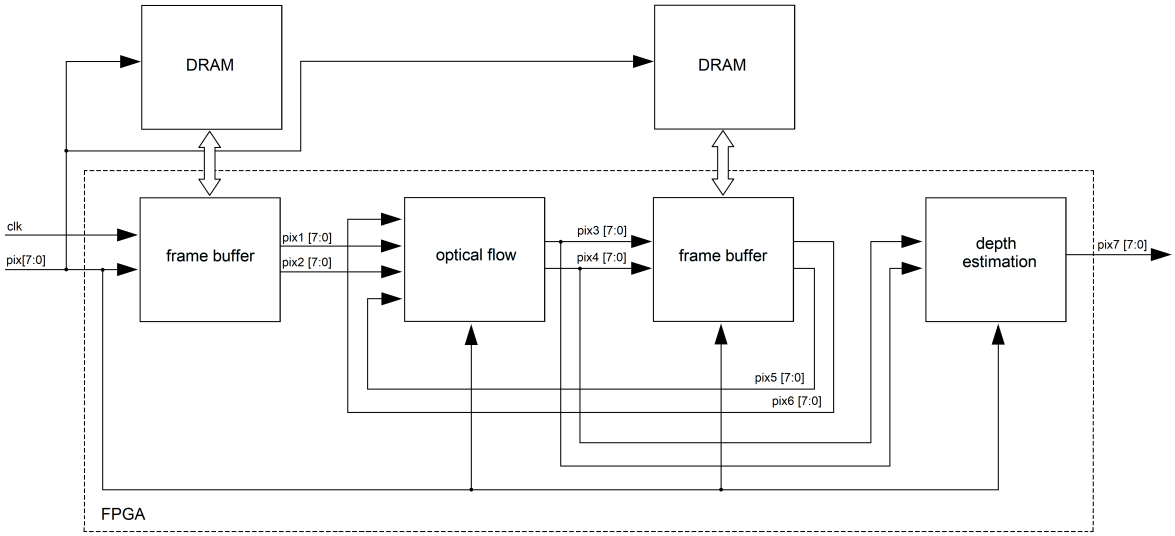

Figure 8. FPGA architecture for the proposed algorithm

4.1. Frame buffer

Images from the image sensor are stored in an external DRAM that holds an entire frame from the sequence, and later the DRAM data is read by the FPGA to cache pixel flow of the stored frame into circular buffers. In order to deliver two consecutive frames in parallel two DRAM chips in switching mode are used. i.e.:

1. t_1: DRAM 1 in write mode (storing frame 1), DRAM 2 in read mode (invalid values), frame 1 at output 1, invalid values at output 2.
2. t_2: DRAM 1 in read mode (reading frame 1), DRAM 2 in write mode (storing frame 1), frame 1 at output 2, frame 1 at output 2.

3. t_3: DRAM 1 in write mode (storing frame 3), DRAM 2 in read mode (reading frame 2), frame 3 at output 2, frame 2 at output 2 and so on.

In **Fig.** 9, an overview of the "frame buffer" unit is shown. Current pixel stream (pix [7:0]) is mapped at output 1 (pix1 [7:0]) while output 2 (pix2 [7:0]) delivers pixel flow for a previous frame. For the external DRAM control, data [7:0] is mapped with the read/write pixel stream, address [31:0] manages the physical location inside the memory and the ”we” and ”re” signals enable the write/read process respectively, as shown in **Fig.** 9.

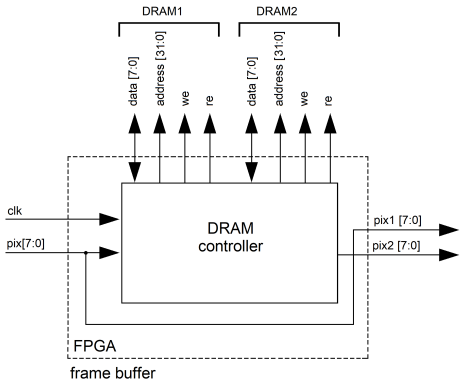

Figure 9. FPGA architecture for the "frame buffer" unit. Two external memories configured in switching mode makes possible to store the current frame (time t) into a DRAM configured in write mode while another DRAM (in read mode) deliver pixel flow for a previous frame (frame at time $t-1$).

4.2. Optical flow

For the "Optical flow" unit, we consider that flow estimation problem can be a generalization of the dense matching problem. i.e., stereo matching algorithms track (searching on the horizontal axis around the search image), all pixels in the reference image. Optical flow aims to track all pixels between two consecutive frames from a video sequence (searching around spatial coordinates of the pixels in the search image). Then, it is possible to extend previous stereo matching FPGA architectures to fulfil with our application domain. In this work, we extended the FPGA architecture presented in [24], since it has low hardware requirements and high parallelism level. In **Fig.** 10, the developed architecture is shown. First, the "curl" units deliver curl images in parallel, see **Eq.** 2. More details about the FPGA architecture of this unit are shown in **Section** 4.2.2. The "circular buffer" units are responsible for data transfers in segments of the image (usually several rows of pixels). So, the core of the FPGA architecture are the circular buffers attached to the local processors that can hold temporarily as cache, for image sections from two frames, and that can deliver parallel data to the processors. More details about the FPGA architecture of this unit are shown in **Section** 4.2.1. Then, given optical flow previously computed, 121 search regions are constructed in parallel, see **Fig.** 5 and **Eq.** 4 - 5. For our implementation, the search region size is equal to 10, therefore, the center of the search regions are all the sampled pixels within the reference region. Given the reference region in $f_t(x,y)$ and 121 search regions in $f_{t+1}(x,y)$, search regions are compared with the reference region (**Eq.** 3) in parallel. For that, a pixel-parallel/window-parallel scheme is implemented. Finally, in the "flow estimation" unit a multiplexer tree can determine the a,b indices that minimize **Eq.** 3, and therefore, the optical flow for all pixels in the reference image, using **Eq.** 6.

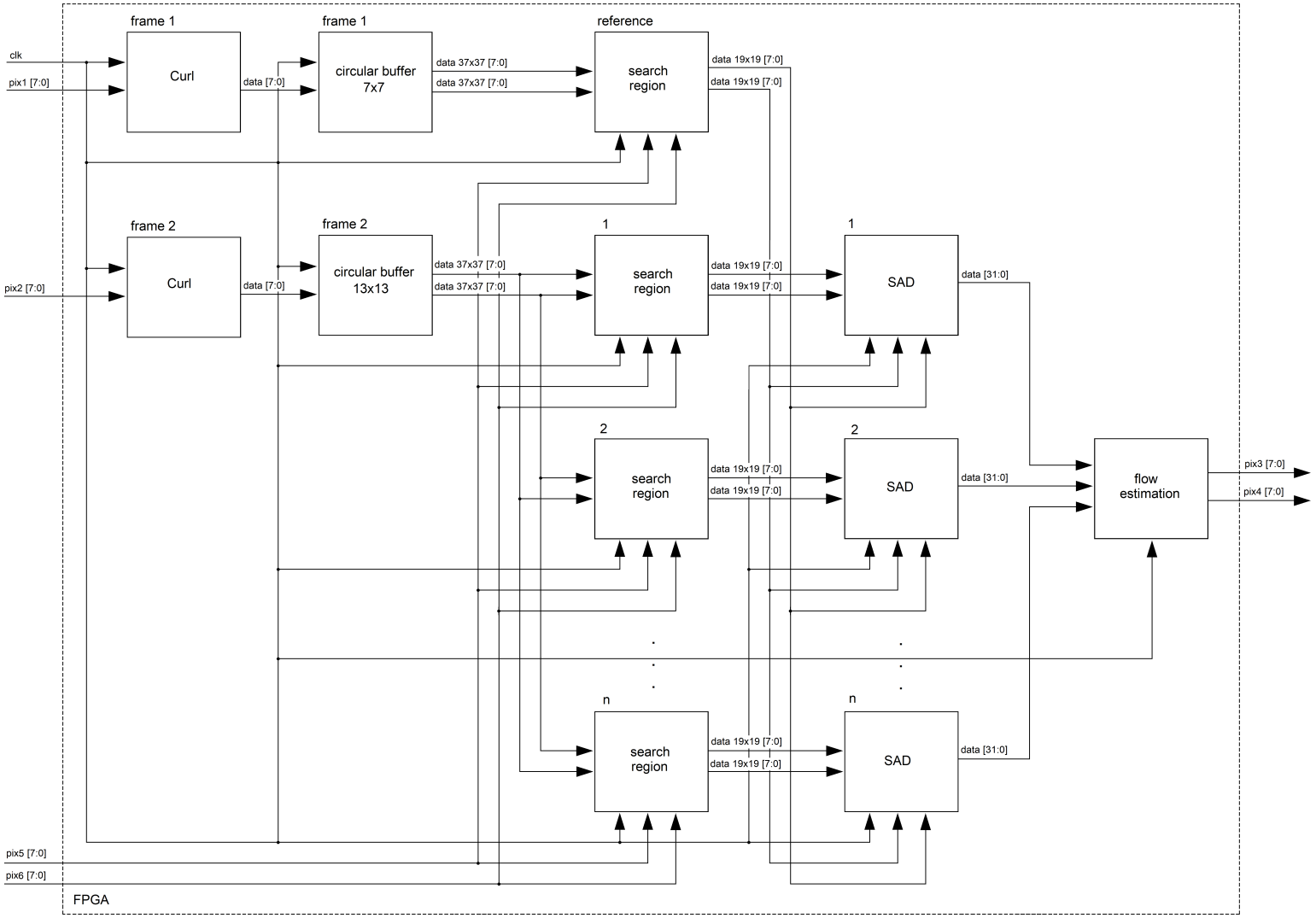

Figure 10. FPGA architecture for the optical flow estimation

4.2.1. Circular buffer

In [23] we proposed a circular buffer schema in which input data from the previous n rows of an image can be stored using memory buffers (block RAMs/BRAMs) until the moment when a $n \times n$ neighborhood is scanned along subsequent rows. In this work, we follow a similar approach to achieve high data reuse and high level of parallelism. Then, our algorithm is processed in modules where all image patches can be read in parallel. First, a shift mechanism "control" unit manages the read/write addresses of $n+1$ BRAMs, in this formulation n BRAMs are in read mode and one BRAM is in write mode in each clock cycle. Then, data inside the read mode BRAMs can be accessed in parallel and each pixel within a $n \times n$ region is delivered in parallel a $n \times n$ buffer, as shown in **Fig.** 11, where the "control" unit delivers control data (address and read/write enable) for the BRAM modules, one entire row is stored in each BRAM. Finally the "data" unit delivers $n \times n$ pixels in parallel. In our implementation, there is 1 circular buffer of 13×13 pixels/bytes, 1 circular buffer of 17×17 and 2 circular buffers of 3×3. For more details see [23].

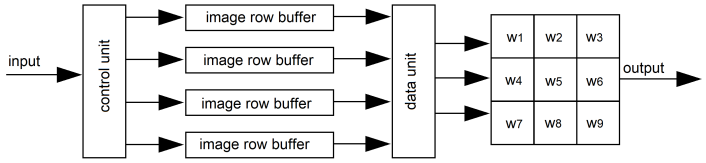

(a) General formulation of a 3 × 3 circular buffer

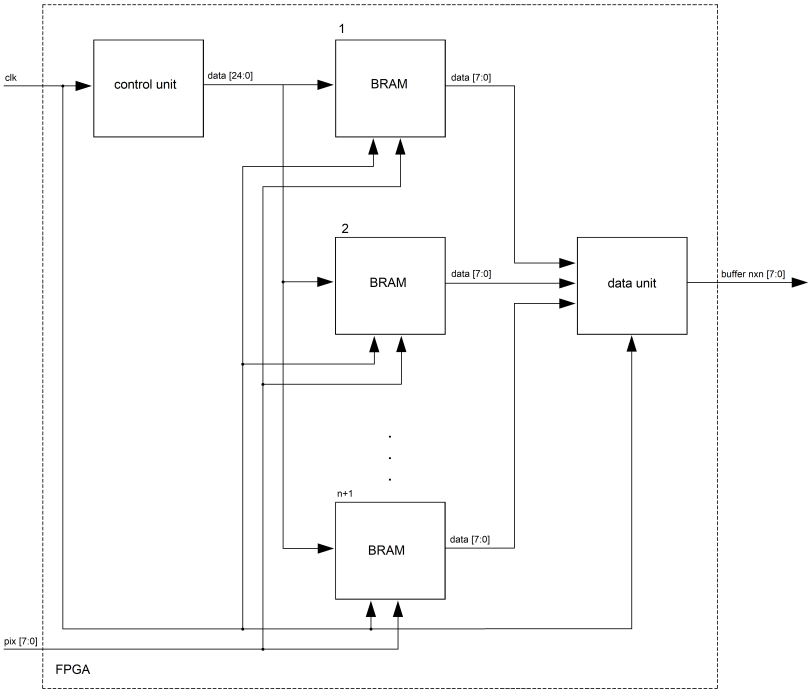

(b) FPGA architecture for the circular buffers

Figure 11. The circular buffers architecture. For a $n \times n$ patch, a shift mechanism "control" unit manages the read/write addresses of $n+1$ BRAMs. In this formulation n BRAMs are in read mode and one BRAM is in write mode in each clock cycle. Then, the $n \times n$ buffer delivers logic registers with all pixels within the patch in parallel.

4.2.2. Curl estimation

In **Fig.** 12, the curl architecture is shown. First, one "circular buffer" holds 3 rows of the frame being processed and allows for local parallel access of a 3×3 patch that facilitates parallel processing. Then, image gradients ($\frac{\partial f(x,y)}{\partial x}$, $\frac{\partial f(x,y)}{\partial y}$) are computed. Another "circular buffer" holds 3 rows of the gradient image previously computed and delivers a 3×3 patch for the next step. Second derivatives ($\frac{\partial}{\partial y}\frac{\partial f(x,y)}{\partial x}$, $\frac{\partial}{\partial x}\frac{\partial f(x,y)}{\partial y}$) are computed inside the "derivative" unit. Finally, the curl of the input image is computed by the "curl" unit.

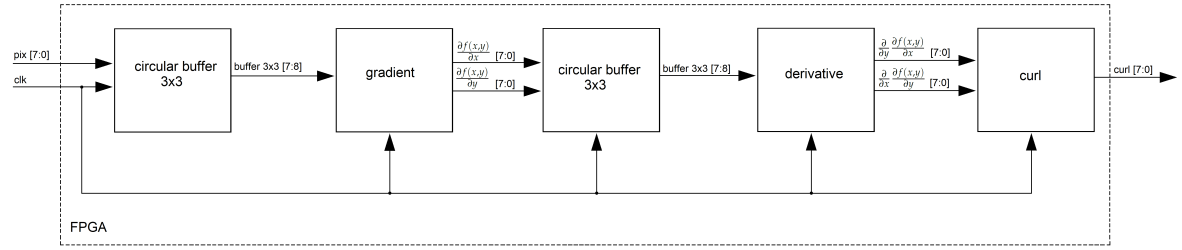

Figure 12. FPGA architecture for the "curl" unit

4.3. Depth estimation

In **Fig.** 13, the depth estimation architecture is shown. Let "pix1 [7;0]", "pix2 [7:0]" be the pixel stream for the optical flow at current frame (**Eq.** 6); first, the "multiplier" unit computes the square value of the input data. Then, the "adder" unit carries out the addition process for both components (Δ_x^2, Δ_y^2). Finally, the "sqrt" unit computes the depth in the scene, using **Eq.** 9. In order to achieve high efficiency in the square root computation, we adapted the architecture developed by Yamin Li and Wanming Chu [38]. This architecture uses a shift register mechanism and compares the more significant/less significant bits to achieving the root square operation without using embedded multipliers.

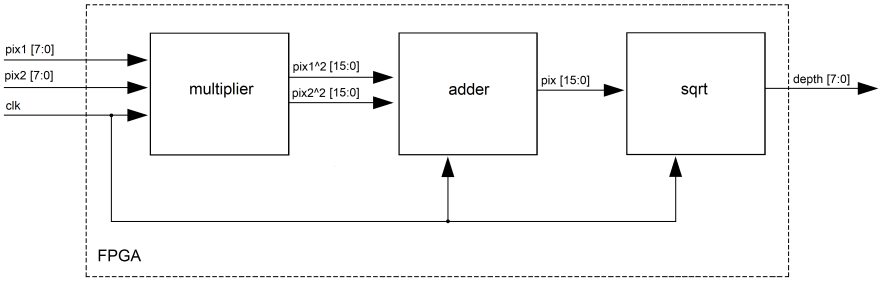

Figure 13. FPGA architecture for the "depth estimation" unit

5. Result and discussion

The developed FPGA architecture was implemented in an FPGA Cyclone IV EP4CGX150CF23C8 of Altera. All modules were designed via Quartus II Web Edition version 10.1SP1 and, all modules were validated via post-synthesis simulations performed in ModelSim Altera. For all tests, we consider $k = 3$, $s = 2$ (**Eq.** 4 and 5) since these values provided a relatively "good" performance for real world scenarios . In practice, we recommend these values as reference. Higher $k = 3$, $s = 2$ values could provide higher accuracy, however, processing speed and hardware requirements can be increased. On the other hand, lower $k = 3$, $s = 2$ values should provide higher performance in terms of hardware requirements /processing speed but accuracy could decrease. The full hardware resource consumption of the architecture is shown in **Table** 1. Our algorithm formulation allows for a compact system design; it requires 66% of the total logic elements of the FPGA Cyclone IV EP4CGX150CF23C8. For

memory bits, our architecture uses 74% of the total resources, this represents 26 block RAMs consumed mainly in the circular buffers. These hardware utilization enables to target a relatively small FPGA device and therefore could be possible a small FPGA-based smart camera, suitable for real-time embedded applications. In the following subsections comparisons with previous work are presented. For optical flow, comparisons with previous FPGA-based optical flow algorithms are presented. For depth estimation, we presented a detailed discussion about the performance and limitations of the proposed algorithm compared with the current state of the art.

5.1. Performance for the optical flow algorithm

Table 1. Hardware resource consumption for the developed FPGA architecture.

Resource	Consumption/image resolution		
	640×480	**320×240**	**256×256**
Total logic elements	69,879 (59%)	37,059 (31%)	21,659 (18%)
Total pins	16 (3%)	16 (3%)	16 (3%)
Total Memory Bits	618,392 (15%)	163,122 (4%)	85,607 (2%)
Embedded multiplier elements	0 (0%)	0 (0%)	0 (0%)
Total PLLs	1 (25%)	1 (25%)	1 (25%)

In comparison with previous work, in **Table** 2 we present hardware resource utilization between our FPGA architecture and previous FPGA-based optical flow algorithms. There are several works [22,25–27] whose FPGA implementations aims to parallelize all recursive operations in the original mathematical formulation. Unfortunately, most popular formulations such as those based in KTL [28] or Horn-Schunck [33], have iterative operations that are hard to parallelize. As result, most previous works have relatively high hardware occupancy/implementations compared with a full parallelizable design approach. Compared with previous works, our FPGA architecture outperform most previous works, for similar image resolution, less logic elements and memory bits than [25,29], and less logic elements and memory bits than [27]. [27] decreases the memory usage by a multiscale coding which makes possible to store only half of the original image, however, this reduction involves pixel interpolation for some cases and this increases the logic elements usage. For [22], the authors introduced an iterative-parallel approach; this makes possible to achieve low hardware requirements but processing speed is low. Finally, for [26], a filtering-based approach makes possible to achieve low hardware requirements with relatively high accuracy and high processing speed but the algorithmic formulation requires to store several entire frames, requiring large external memory (near 250 MB for store 3 entire frames), this increase the system size and cost.

Table 2. Hardware resource consumption comparisons

Method	**Logic elements**	**Memory bits**	**Image resolution**
Martín *et al.* [22] (2005)	11,520	147,456	256×256
Díaz *et al.* [25] (2006)	513,216	685,670	320×240
Wei *et al.* [26] (2007)	10,288	256 MB (DDR)	640×480
Barranco *et al.* [27] (2012)	82,526	573,440	640×480
Honegger *et al.* [29] (2012)	49,655	1,111,000	376×240
Our work*	69,879	624,244	640×480
Our work*	37,059	163,122	320×240
Our work*	21,659	85,607	256×256

*Operating frequency = 50 MHz

In **Table** 3, speed processing for different image resolutions is shown. We synthesized different versions of our FPGA architecture (**Fig.** 8), and we adapted the circular buffers in order to work with all tested image resolutions. Then, we carried out post-synthesis simulation in ModelSim Altera. In all cases, our FPGA architecture reached real-time processing. When compared with previous work (**Table** 4), our algorithm provided the highest speed processing, it outperforms several previous work [22,25–27,29], and for HD images, our algorithm reaches real-time processing: more than 60 fps for 1280×1024 image resolution.

Table 3. Processing speed for different image resolutions

Resolution	Frames/s	Pixels/s
1280×1024	68	90,129,200
640×480	297	91,238,400
320×240	1,209	92,880,000
256×256	1,417	92,876,430

*Operating frequency = 50 MHz

Table 4. Processing speed comparisons

Method	Resolution	Frames/s	Pixels/s
Martín *et al.* [22]	256×256	60	3,932,160
Díaz *et al.* [25]	320×240	30	2,304,000
Wei *et al.* [26]	640×480	64	19,550,800
Barranco *et al.* [27]	640×480	31	9,523,200
Honegger *et al.* [29]	376×240	127	11,460,480
Our work	640×480	297	91,238,400

In **Fig.** 14, qualitative results for this work compared with previous work are shown. In a first experiment we used the "Garden" dataset since previous work [22,25,26] used this dataset as reference. When compared with previous work (**Fig.** 14), our algorithm provides high performance under real world scenarios, it outperforms several previous work [22,25,26], quantitatively closer to the ground truth (error near to 9%) compared with other FPGA-based approaches. In a second experiment quantitative and qualitative results for the KITTI dataset [39], are shown. In all cases our algorithm provides high performance, it reaches an error near to 10% with several test sequences, as shown in **Fig.** 15. In both experiments we compute the error by comparing the ground truth $\Omega_x(x,y)$, $\Omega_y(x,y)$ (provided with the dataset) with the computed optical flow $\Delta_x(x,y)$, $\Delta_y(x,y)$. First, we compute the local error (the error magnitude at each point of the input image) as defined in **Eq.** 10; where i,j is the input image resolution. Then, a global error (Ξ) can be computed as shown in **Eq.** 11; where i,j is the input image resolution. $\xi(x,y)$ is the local error at each pixel in the reference image and the global error (Ξ) is the percentage of pixels in the reference image in which local error is higher to zero.

$$\xi(x,y) = \sum_{x=1}^{x=i}\sum_{y=1}^{y=j}\sqrt{\Omega_x(x,y)^2+\Omega_y(x,y)^2} - \sqrt{\Delta_x(x,y)^2+\Delta_y(x,y)^2} \tag{10}$$

$$\Xi = \frac{100\%}{i\cdot j}\cdot\sum_{x=1}^{x=i}\sum_{y=1}^{y=j}\begin{cases}1 & if\ \xi(x,y) >= 0\\ 0 & otherwise\end{cases} \tag{11}$$

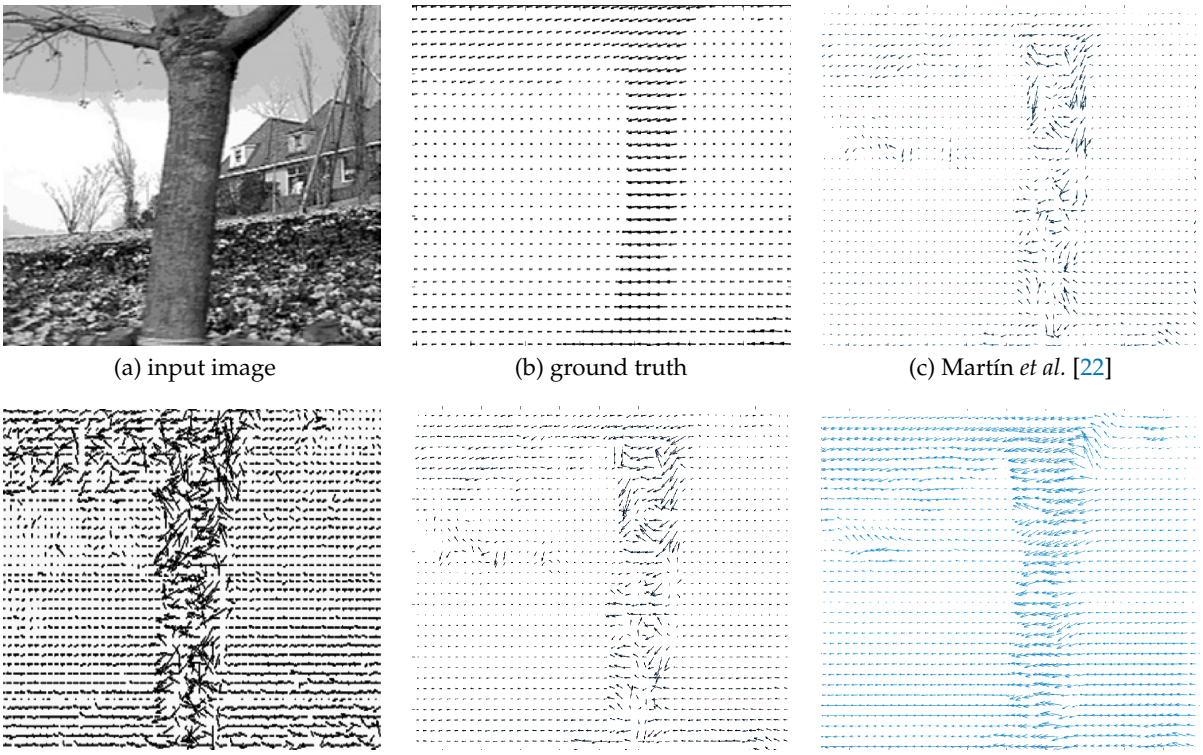

(a) input image (b) ground truth (c) Martín *et al.* [22]

(d) Wei *et al.* [26] (e) Díaz *et al.* [25] (f) this work (error = 9%)

Figure 14. Accuracy performance for different FPGA-based optical flow algorithms.

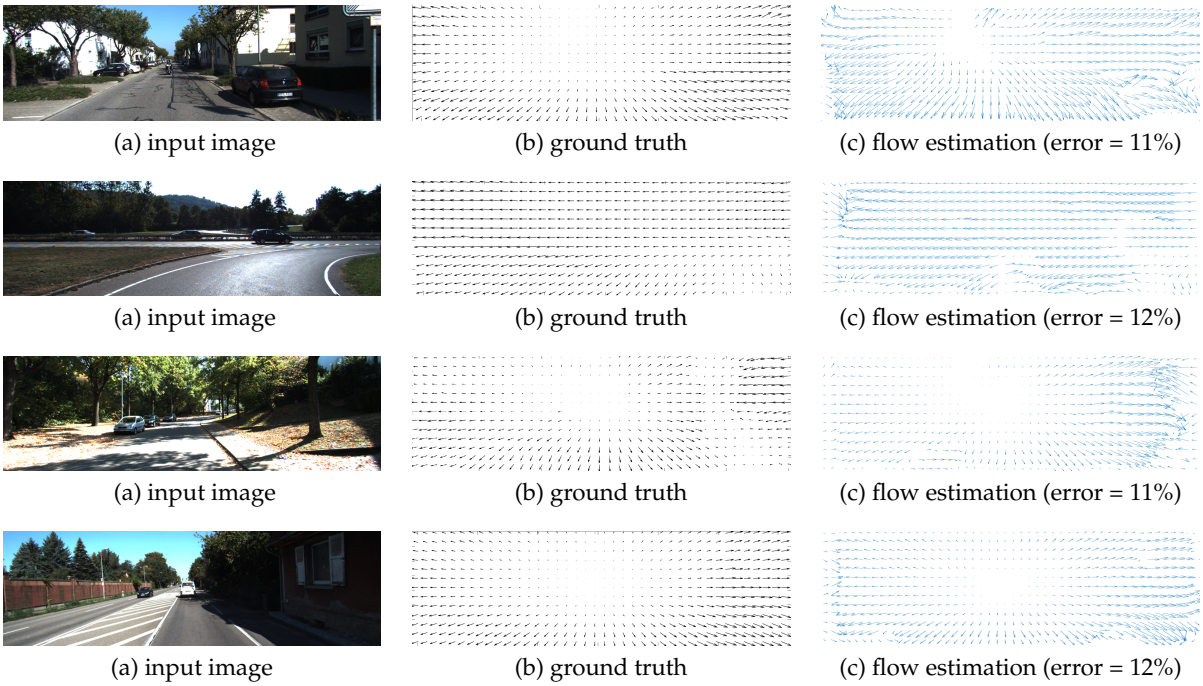

(a) input image (b) ground truth (c) flow estimation (error = 11%)

(a) input image (b) ground truth (c) flow estimation (error = 12%)

(a) input image (b) ground truth (c) flow estimation (error = 11%)

(a) input image (b) ground truth (c) flow estimation (error = 12%)

Figure 15. Optical flow: quantitative/qualitative results for the KITTI dataset

5.2. *Performance for the depth estimation step*

In **Fig.** 15, quantitative and qualitative results for the KITTI dataset [39], are shown. In all cases our algorithm provides rough depth maps compared with stereo-based or deep learning approaches [40,41] but with real-time processing and with the capability to be implemented in embedded hardware, suitable for smart cameras. To our knowledge, previous FPGA-based approaches are limited; there are several GPU-based approaches but in these cases most of the effort was for accuracy improvements and real-time processing or embedded capabilities were not considered so, in several cases, details about the hardware requirements or the processing speed are not provided [42–44]. In **Table** 5 quantitative comparisons between our algorithm and the current state of the art are presented. For previous works, the RMS error, hardware specifications and processing speed were obtained from the published manuscripts while for our algorithm we computed the RMS error as indicated by the KITTI dataset, [45]. For accuracy comparisons, most previous works [42–44,46–48] outperform our algorithm (near 15% more accurate than ours); however, our algorithm outperform all of them in terms of processing speed (a processing speed up to 128 times faster than previous works) and with embedded capabilities (making it possible to develop a smart camera/sensor suitable for embedded applications).

Table 5. Depth estimation process in the literature: performance and limitations for the KITTI dataset.

Method	Error (RMS)	Speed	Image resolution	Approach	
Zhou *et al.* [42](2017)	6.8%	-	128×416	DfM-based*	-
Yang *et al.* [46](2017)	6.5%	5 fps	128×416	CNN-based*	GTX 1080 (GPU)
Mahjourian *et al.* [47](2018)	6.2%	100 fps	128×416	DfM-based*	Titan X (GPU)
Yang *et al.* [43](2018)	6.2%	-	830×254	DfM-based*	Titan X (GPU)
Godard *et al.* [44](2018)	5.6%	-	192×640	CNN-based*	-
Zou *et al.* [48](2018)	5.6%	1.25 fps	576×160	DfM-based*	Tesla K80 (GPU)
Our work	21.5%	192 fps	1241×376	DfM-based	Cyclone IV (FPGA)

*DfM: Depth from Motion, CNN: Convolutional Neural Network

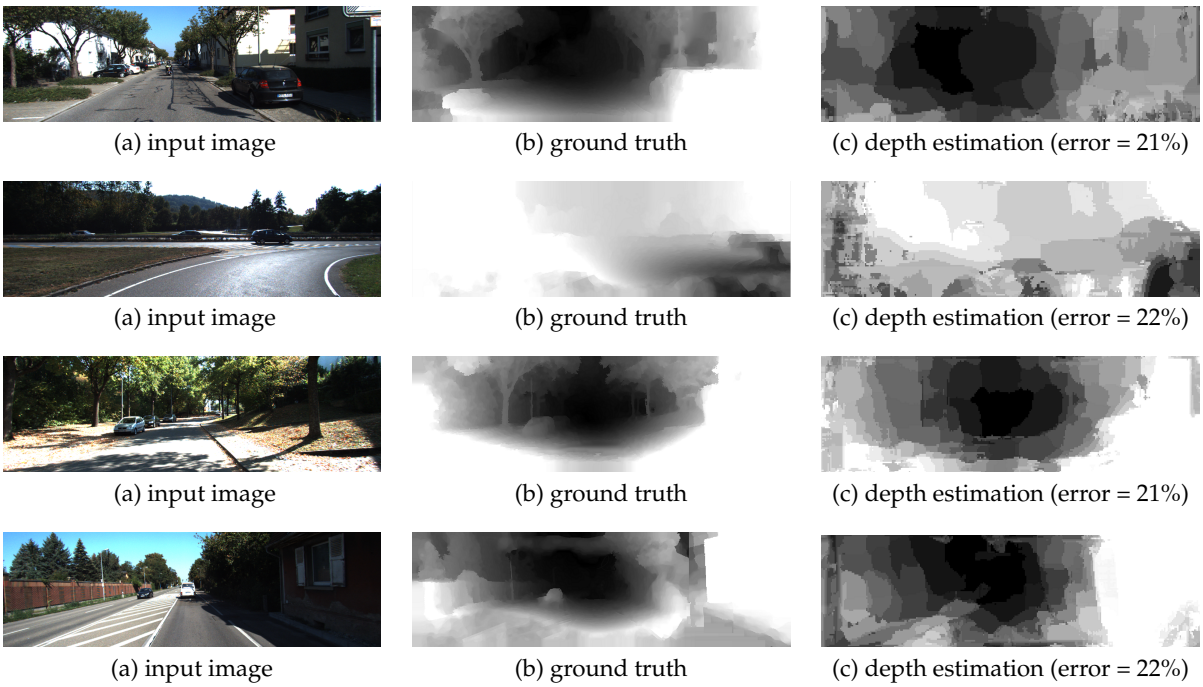

(a) input image (b) ground truth (c) depth estimation (error = 21%)

(a) input image (b) ground truth (c) depth estimation (error = 22%)

(a) input image (b) ground truth (c) depth estimation (error = 21%)

(a) input image (b) ground truth (c) depth estimation (error = 22%)

Figure 16. Depth estimation: quantitative/qualitative results for the KITTI dataset

333 Finally, in **Fig.** 17 an example of 3D reconstruction using our approach is shown. Our depth maps
334 allow for a real-time dense 3D reconstruction. Previous works like the ORB-SLAM [49] or LSD-SLAM
335 [50] compute motion and depth in 2 to 7% of all image pixels, while ours compute 80% of the image
336 pixels. Then, our algorithm improves by around 15 times the current state of the art, making possible
337 real-time dense 3D reconstructions and with the capability to be implemented inside FPGA devices,
338 suitable for smart cameras.
339

(a) Input image

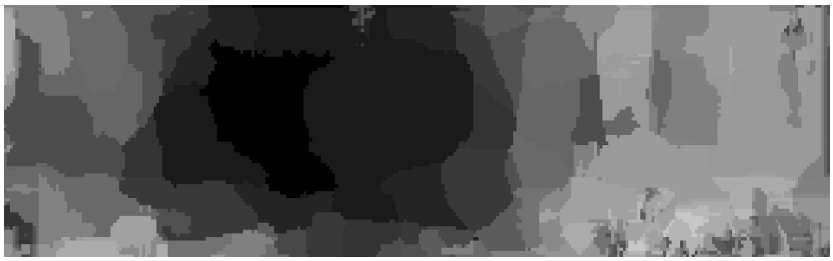

(b) Depth map

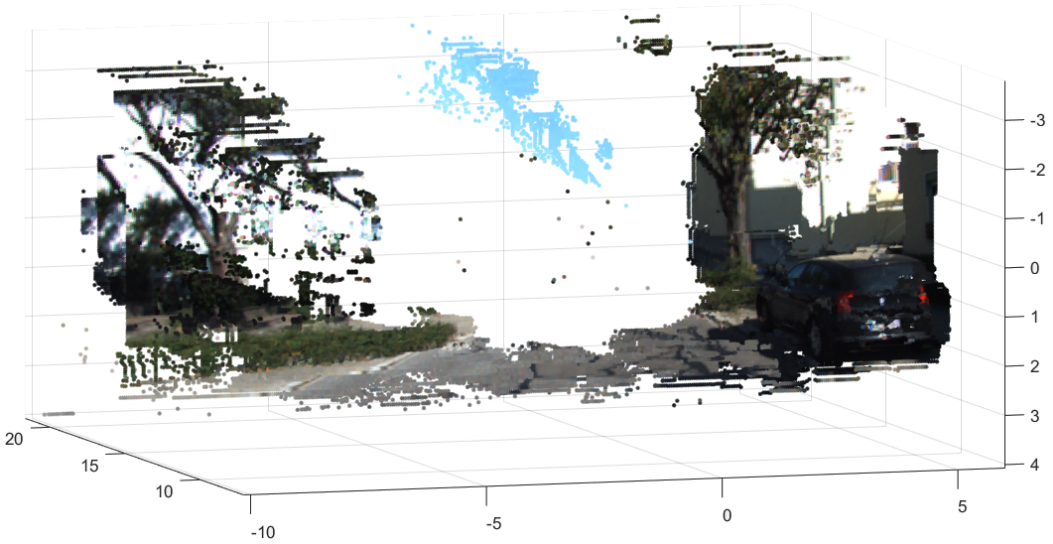

(c) 3D reconstruction

Figure 17. The KITTI dataset: Sequence 00; 3D reconstruction by the proposed approach. Our algorithm provides rough depth maps (lower accuracy compared with previous algorithms) but with real-time processing and with the capability to be implemented in embedded hardware; as result, real-time dense 3D reconstructions can be obtained and, these can be exploited by several real world applications such as, augmented reality, robot vision and surveillance, autonomous flying, etc.

6. Conclusions

Depth from Motion is the problem of depth estimation using information from a single moving camera. Although several Depth from Motion algorithms were developed, previous works have low processing speed and high hardware requirements that limits the embedded capabilities. In order to solve these limitations in this work we have proposed a new depth estimation algorithm whose FPGA implementation deliver high efficiency in terms of algorithmic parallelization. Unlike previous works, depth information is estimated in real time inside a compact FPGA device, making our mathematical formulation suitable for smart embedded applications.

Comparted with the current state of the art, previous algorithms outperform our algorithm in terms of accuracy but our algorithm outperforms all previous approaches in terms of processing speed and hardware requirements; these characteristics makes our approach a promising solutions for the current embedded systems. We believed that several real world applications such as augmented reality, robot vision and surveillance, autonomous flying, etc., can take advantages by applying our algorithm since it delivers real-time depth maps that can be exploited to create dense 3D reconstructions or other abstractions useful for the scene understanding.

Author Contributions: Conceptualization, Abiel Aguilar-González, Miguel Arias-Estrada and François Berry. Investigation, Validation and Writing—Original Draft Preparation: Abiel Aguilar-González. Supervision and Writing—Review & Editing: Miguel Arias-Estrada and François Berry.

Funding: This research received no external funding.

Acknowledgments: This work has been sponsored by the French government research program "Investissements d'avenir" through the IMobS3 Laboratory of Excellence (ANR-10-LABX-16-01), by the European Union through the program Regional competitiveness and employment, and by the Auvergne region. This work has been sponsored by Campus France through the scholarship program "bourses d'excellence EIFFEL", dossier No. MX17-00063 and by the National Council for Science and Technology (CONACyT), Mexico, through the scholarship No. 567804..

Conflicts of Interest: The authors declare no conflict of interest.

1. Hengstler, S.; Prashanth, D.; Fong, S.; Aghajan, H. MeshEye: a hybrid-resolution smart camera mote for applications in distributed intelligent surveillance. Proceedings of the 6th international conference on Information processing in sensor networks. ACM, 2007, pp. 360–369.
2. Aguilar-González, A.; Arias-Estrada, M. Towards a smart camera for monocular SLAM. Proceedings of the 10th International Conference on Distributed Smart Camera. ACM, 2016, pp. 128–135.
3. Carey, S.J.; Barr, D.R.; Dudek, P. Low power high-performance smart camera system based on SCAMP vision sensor. *Journal of Systems Architecture* **2013**, *59*, 889–899.
4. Birem, M.; Berry, F. DreamCam: A modular FPGA-based smart camera architecture. *Journal of Systems Architecture* **2014**, *60*, 519–527.
5. Bourrasset, C.; Maggianiy, L.; Sérot, J.; Berry, F.; Pagano, P. Distributed FPGA-based smart camera architecture for computer vision applications. Distributed Smart Cameras (ICDSC), 2013 Seventh International Conference on. IEEE, 2013, pp. 1–2.
6. Bravo, I.; Baliñas, J.; Gardel, A.; Lázaro, J.L.; Espinosa, F.; García, J. Efficient smart cmos camera based on fpgas oriented to embedded image processing. *Sensors* **2011**, *11*, 2282–2303.
7. Köhler, T.; Röchter, F.; Lindemann, J.P.; Möller, R. Bio-inspired motion detection in an FPGA-based smart camera module. *Bioinspiration & biomimetics* **2009**, *4*, 015008.
8. Olson, T.; Brill, F. Moving object detection and event recognition algorithms for smart cameras. Proc. DARPA Image Understanding Workshop, 1997, Vol. 20, pp. 205–208.
9. Norouznezhad, E.; Bigdeli, A.; Postula, A.; Lovell, B.C. Object tracking on FPGA-based smart cameras using local oriented energy and phase features. Proceedings of the Fourth ACM/IEEE International Conference on Distributed Smart Cameras. ACM, 2010, pp. 33–40.
10. Fularz, M.; Kraft, M.; Schmidt, A.; Kasiński, A. The architecture of an embedded smart camera for intelligent inspection and surveillance. In *Progress in Automation, Robotics and Measuring Techniques*; Springer, 2015; pp. 43–52.

11. Haritaoglu, I.; Harwood, D.; Davis, L.S. W 4: Real-time surveillance of people and their activities. *IEEE Transactions on pattern analysis and machine intelligence* **2000**, *22*, 809–830.
12. Biswas, J.; Veloso, M. Depth camera based indoor mobile robot localization and navigation. Robotics and Automation (ICRA), 2012 IEEE International Conference on. IEEE, 2012, pp. 1697–1702.
13. Stowers, J.; Hayes, M.; Bainbridge-Smith, A. Altitude control of a quadrotor helicopter using depth map from Microsoft Kinect sensor. Mechatronics (ICM), 2011 IEEE International Conference on. IEEE, 2011, pp. 358–362.
14. Scharstein, D.; Szeliski, R. A taxonomy and evaluation of dense two-frame stereo correspondence algorithms. *International journal of computer vision* **2002**, *47*, 7–42.
15. Subbarao, M.; Surya, G. Depth from defocus: a spatial domain approach. *International Journal of Computer Vision* **1994**, *13*, 271–294.
16. Chen, Y.; Alain, M.; Smolic, A. Fast and accurate optical flow based depth map estimation from light fields. Irish Machine Vision and Image Processing Conference (IMVIP), 2017.
17. Zhang, J.; Singh, S. Visual-lidar odometry and mapping: Low-drift, robust, and fast. Robotics and Automation (ICRA), 2015 IEEE International Conference on. IEEE, 2015, pp. 2174–2181.
18. Schubert, S.; Neubert, P.; Protzel, P. Towards camera based navigation in 3d maps by synthesizing depth images. Conference Towards Autonomous Robotic Systems. Springer, 2017, pp. 601–616.
19. Maddern, W.; Newman, P. Real-time probabilistic fusion of sparse 3d lidar and dense stereo. Intelligent Robots and Systems (IROS), 2016 IEEE/RSJ International Conference on. IEEE, 2016, pp. 2181–2188.
20. Dai, A.; Chang, A.X.; Savva, M.; Halber, M.; Funkhouser, T.A.; Nießner, M. ScanNet: Richly-Annotated 3D Reconstructions of Indoor Scenes. **2017**. *2*, 10.
21. Liu, H.; Li, C.; Chen, G.; Zhang, G.; Kaess, M.; Bao, H. Robust Keyframe-based Dense SLAM with an RGB-D Camera. *arXiv preprint arXiv:1711.05166* **2017**.
22. Martín, J.L.; Zuloaga, A.; Cuadrado, C.; Lázaro, J.; Bidarte, U. Hardware implementation of optical flow constraint equation using FPGAs. *Computer Vision and Image Understanding* **2005**, *98*, 462–490.
23. Aguilar-González, A.; Arias-Estrada, M.; Pérez-Patricio, M.; Camas-Anzueto, J. An FPGA 2D-convolution unit based on the CAPH language. *Journal of Real-Time Image Processing* **2015**, pp. 1–15.
24. Pérez-Patricio, M.; Aguilar-González, A.; Arias-Estrada, M.; Hernandez-de Leon, H.R.; Camas-Anzueto, J.L.; de Jesús Osuna-Coutiño, J. An fpga stereo matching unit based on fuzzy logic. *Microprocessors and Microsystems* **2016**, *42*, 87–99.
25. Díaz, J.; Ros, E.; Pelayo, F.; Ortigosa, E.M.; Mota, S. FPGA-based real-time optical-flow system. *IEEE transactions on circuits and systems for video technology* **2006**, *16*, 274–279.
26. Wei, Z.; Lee, D.J.; Nelson, B.E. FPGA-based Real-time Optical Flow Algorithm Design and Implementation. *Journal of Multimedia* **2007**, *2*.
27. Barranco, F.; Tomasi, M.; Diaz, J.; Vanegas, M.; Ros, E. Parallel architecture for hierarchical optical flow estimation based on FPGA. *IEEE Transactions on Very Large Scale Integration (VLSI) Systems* **2012**, *20*, 1058–1067.
28. Tomasi, C.; Kanade, T. Detection and tracking of point features. *School of Computer Science, Carnegie Mellon Univ. Pittsburgh* **1991**.
29. Honegger, D.; Greisen, P.; Meier, L.; Tanskanen, P.; Pollefeys, M. Real-time velocity estimation based on optical flow and disparity matching. IROS, 2012, pp. 5177–5182.
30. Chao, H.; Gu, Y.; Napolitano, M. A survey of optical flow techniques for robotics navigation applications. *Journal of Intelligent & Robotic Systems* **2014**, *73*, 361–372.
31. Dosovitskiy, A.; Fischer, P.; Ilg, E.; Hausser, P.; Hazirbas, C.; Golkov, V.; Van Der Smagt, P.; Cremers, D.; Brox, T. Flownet: Learning optical flow with convolutional networks. Proceedings of the IEEE International Conference on Computer Vision, 2015, pp. 2758–2766.
32. Ilg, E.; Mayer, N.; Saikia, T.; Keuper, M.; Dosovitskiy, A.; Brox, T. Flownet 2.0: Evolution of optical flow estimation with deep networks. IEEE conference on computer vision and pattern recognition (CVPR), 2017, Vol. 2, p. 6.
33. Horn, B.K.; Schunck, B.G. Determining optical flow. *Artificial intelligence* **1981**, *17*, 185–203.
34. Khaleghi, B.; Shahabi, S.M.A.; Bidabadi, A. Performace evaluation of similarity metrics for stereo corresponce problem. Electrical and Computer Engineering, 2007. CCECE 2007. Canadian Conference on. IEEE, 2007, pp. 1476–1478.

35. Geiger, A.; Lenz, P.; Stiller, C.; Urtasun, R. Vision meets robotics: The KITTI dataset. *The International Journal of Robotics Research* **2013**, *32*, 1231–1237.
36. Baker, S.; Scharstein, D.; Lewis, J.; Roth, S.; Black, M.J.; Szeliski, R. A database and evaluation methodology for optical flow. *International Journal of Computer Vision* **2011**, *92*, 1–31.
37. Fortun, D.; Bouthemy, P.; Kervrann, C. Optical flow modeling and computation: a survey. *Computer Vision and Image Understanding* **2015**, *134*, 1–21.
38. Li, Y.; Chu, W. A new non-restoring square root algorithm and its VLSI implementations. Computer Design: VLSI in Computers and Processors, 1996. ICCD'96. Proceedings., 1996 IEEE International Conference on. IEEE, 1996, pp. 538–544.
39. Geiger, A.; Lenz, P.; Stiller, C.; Urtasun, R. Vision meets robotics: The KITTI dataset. *The International Journal of Robotics Research* **2013**, *32*, 1231–1237.
40. Fu, H.; Gong, M.; Wang, C.; Batmanghelich, K.; Tao, D. Deep Ordinal Regression Network for Monocular Depth Estimation. IEEE Conference on Computer Vision and Pattern Recognition (CVPR); , 2018.
41. Bo Li, Yuchao Dai, M.H. Monocular Depth Estimation with Hierarchical Fusion of Dilated CNNs and Soft-Weighted-Sum Inference **2018**.
42. Zhou, T.; Brown, M.; Snavely, N.; Lowe, D.G. Unsupervised learning of depth and ego-motion from video. CVPR, 2017, Vol. 2, p. 7.
43. Yang, Z.; Wang, P.; Wang, Y.; Xu, W.; Nevatia, R. LEGO: Learning Edge with Geometry all at Once by Watching Videos. Proceedings of the IEEE Conference on Computer Vision and Pattern Recognition, 2018, pp. 225–234.
44. Godard, C.; Mac Aodha, O.; Brostow, G. Digging Into Self-Supervised Monocular Depth Estimation. *arXiv preprint arXiv:1806.01260* **2018**.
45. Uhrig, J.; Schneider, N.; Schneider, L.; Franke, U.; Brox, T.; Geiger, A. Depth Prediction Evaluation. http://www.cvlibs.net/datasets/kitti/eval_odometry_detail.php?&result=fee1ecc5afe08bc002f093b48e9ba98a295a79ed, 2017.
46. Yang, Z.; Wang, P.; Xu, W.; Zhao, L.; Nevatia, R. Unsupervised Learning of Geometry with Edge-aware Depth-Normal Consistency. *arXiv preprint arXiv:1711.03665* **2017**.
47. Mahjourian, R.; Wicke, M.; Angelova, A. Unsupervised Learning of Depth and Ego-Motion from Monocular Video Using 3D Geometric Constraints. Proceedings of the IEEE Conference on Computer Vision and Pattern Recognition, 2018, pp. 5667–5675.
48. Zou, Y.; Luo, Z.; Huang, J.B. Df-net: Unsupervised joint learning of depth and flow using cross-task consistency. European Conference on Computer Vision. Springer, 2018, pp. 38–55.
49. Mur-Artal, R.; Montiel, J.M.M.; Tardos, J.D. ORB-SLAM: a versatile and accurate monocular SLAM system. *IEEE Transactions on Robotics* **2015**, *31*, 1147–1163.
50. Engel, J.; Schöps, T.; Cremers, D. LSD-SLAM: Large-scale direct monocular SLAM. European Conference on Computer Vision. Springer, 2014, pp. 834–849.

Sample Availability: Samples of the compounds ..... are available from the authors.